CHEMISTRY OF MATERIALS

Article

pubs.acs.org/cm

Semiconducting Pavonites $CdMBi_4Se_8$ (M = Sn and Pb) and Their Thermoelectric Properties

Jing Zhao,[†,‡] Saiful M. Islam,[‡] Shiqiang Hao,[§] Gangjian Tan,[‡] Xianli Su,[‡,∥] Haijie Chen,[‡] Wenwen Lin,[‡] Rukang Li,[†] Chris Wolverton,[§] and Mercouri G. Kanatzidis*,[‡]

[†]Beijing Center for Crystal Research and Development, Technical Institute of Physics and Chemistry, Chinese Academy of Sciences, Beijing 100190, P. R. China

[‡]Department of Chemistry, Northwestern University, Evanston, Illinois 60208, United States

[§]Department of Materials Science and Engineering, Northwestern University, Evanston, Illinois 60208, United States

[∥]State Key Laboratory of Advanced Technology for Materials Synthesis and Processing, Wuhan University of Technology, Wuhan 430070, China

Supporting Information

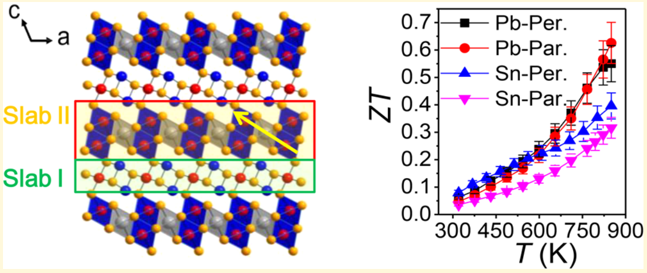

ABSTRACT: Two new compounds $CdPbBi_4Se_8$ and $CdSnBi_4Se_8$ adopt the pavonite structure type and crystallize in the monoclinic space group $C2/m$ with a = 13.713(3) Å, b = 4.1665(8) Å, c = 15.228(3) Å, β = 115.56(3)° for $CdPbBi_4Se_8$; a = 13.679 Å, b = 4.153 Å, c = 15.127 Å, β = 115.51° for $CdSnBi_4Se_8$. Their crystal structures are composed of two different types of polyhedral slabs, one containing a mixture of one octahedron [MSe_6] block and paired squared pyramids [MSe_5], while the other forms distorted galena-type (or NaCl-type) lattices with three [MSe_6] octahedral chains (M = Pb, Cd, Bi, Sn). Both $CdPbBi_4Se_8$ and $CdSnBi_4Se_8$ are stable up to ~970 K. Density functional theory (DFT) calculations show that both $CdPbBi_4Se_8$ and $CdSnBi_4Se_8$ are indirect band gap semiconductors. DFT phonon dispersion calculations performed on $CdSnBi_4Se_8$ give valuable insights as to the origin of the observed low experimental lattice thermal conductivities of ~0.58 W m^{-1} K^{-1} at 320 K. The title compounds exhibit n-type conduction, and they exhibit promising thermoelectric properties with a maximum thermoelectric figure of merit, ZT, reaching 0.63 for $CdPbBi_4Se_8$, and 0.40 for $CdSnBi_4Se_8$ at 850 K.

INTRODUCTION

Thermoelectric materials, which can be used to convert waste heat to electricity or generate cooling via the Peltier effect, provide a more efficient means of energy usage and conversion.[1−3] Thermoelectric materials with large values of figure of merit ZT = $S^2\sigma T/\kappa$ are necessary for efficient thermoelectric devices, where T is the operating temperature, S is the Seebeck coefficient or thermopower, σ is the electrical conductivity, and κ is the thermal conductivity. From the formula, the current challenge lies in achieving a high power factor (σS^2) and a low thermal conductivity (κ) simultaneously in one material.

There are several alternatives to improving ZT are either using all-scale hierarchical materials engineering of existing materials or searching for developing completely new compounds that may exhibit high thermoelectric performance.[4,5] Among the high-ZT materials, lead or tin chalcogenides and their alloys with other chalcogenides are the most efficient ones for power generation applications at high temperature.[6−9] There are several large bismuth containing chalcogenide homologous families which have been shown to be great sources for narrow band gap semiconductors that are promising as efficient thermoelectric materials. These include the $A_m[M_{1+l}Se_{2+l}]_{2m}[M_{2l+n}Se_{2+3l+n}]$ (A = alkali metal, M = Sn or Bi)[10−12] and $CsBi_{4+2m}Te_{6+3m}$ families[13] which have produced $K_2Bi_8Se_{13}$ and $CsBi_4Te_6$ as excellent thermoelectrics. The main reason for this high performance is the complex anisotropic crystal structures of these compounds which tend to exhibit very low thermal conductivities. Another such great homologous series is the so-called pavonite family, but there is a dearth of data on the electrical and thermal transport properties in this series. Like pavonite, there are some other examples of minerals with thermoelectric properties explored, such as $Pb_5Bi_6Se_{14}$, a member of the cannizzarite homologous series; $PbBi_2S_4$, a member of the galenobismuthite homologous series; $Pb_3Bi_2S_6$, a member of the lillianite homologous series;[14] and $Cu_{12}Sb_4S_{13}$, a derivative of tetrahedrite.[15,16]

The minerals of the pavonite structure are from one of the most prolific homologous series known.[17] Pavonite structures are three-dimensional (3D) but anisotropic and are composed of two alternating types of slabs: one features single MQ_6 (Q =

Received: August 7, 2017
Revised: September 11, 2017
Published: September 11, 2017

DOI: 10.1021/acs.chemmater.7b03328
Chem. Mater. 2017, 29, 8494−8503

Table 1. Crystal Data and Structural Refinement Statistics for $CdPbBi_4Se_8$ and $CdSnBi_4Se_8$ at 293(2) K[a]

empirical formula	$CdPbBi_4Se_8$	$CdSnBi_4Se_8$
fw	1785.58	1698.69
cryst syst	monoclinic	monoclinic
space group	$C2/m$	$C2/m$
unit cell dimensions	$a = 13.713(3)$ Å, $b = 4.1665(8)$ Å, $c = 15.228(3)$ Å, $\beta = 115.56(3)°$	$a = 13.679(1)$ Å, $b = 4.1528(3)$ Å, $c = 15.4178(13)$ Å, $\beta = 115.51°$
V (Å^3)	784.9(3)	775.5
Z	2	2
density (calcd) (g/cm^3)	7.555	7.274
abs coeff (mm^{-1})	75.210	66.888
$F(000)$	1467	1404
cryst size (mm^3)	0.049 × 0.034 × 0.02	0.347 × 0.054 × 0.07
θ range for data collection (deg)	2.966−29.132°	2.979−29.144°
index ranges	$-18 \le h \le 18$, $-5 \le k \le 5$, $-20 \le l \le 20$	$-18 \le h \le 18$, $-5 \le k \le 5$, $-17 \le l \le 20$
reflns collected	3751	3759
indep reflns	1195 [$R_{int} = 0.0499$]	1142 [$R_{int} = 0.0370$]
completeness to $\theta = 24.96°$	99.8%	98.4%
data/restraints/params	1195/0/46	1142/0/48
refinement method	full-matrix least-squares on F^2	
GOF	1.066	1.086
final R indices [$>2\sigma(I)$]	$R_1 = 0.0399$, $wR_1 = 0.0904$	$R_1 = 0.0312$, $wR_1 = 0.0580$
R indices [all data]	$R_2 = 0.0484$, $wR_2 = 0.0936$	$R_2 = 0.0433$, $wR_2 = 0.0609$
largest difference peak and hole (e Å^{-3})	5.393 and −2.582	1.629 and −1.859

[a] $R = \sum||F_o| - |F_c||/\sum|F_o|$, $wR = \{\sum[w(|F_o|^2 - |F_c|^2)^2]/\sum[w(|F_o|^4)]\}^{1/2}$, and $w = 1/[\sigma^2(F_o^2) + (0.1000P)^2]$ where $P = (F_o^2 + 2F_c^2)/3$.

S and Se) octahedra and alternating with columns of paired square MQ_5 pyramids; the other one is slab of galena-like structure with a variable thickness. Members of this series have a general chemical formula $M_{N+1}Bi_2Q_{N+5}$, in which M is six coordinated metals, such as Li^+, Na^+, Ag^+, Cu^+, Pb^{2+}, Cd^{2+}, Hg^{2+}, Mn^{2+}, In^{3+}, Bi^{3+}, and Sb^{3+}, and Q can be S, Se, or Cl.[17] N is the number of octahedra per one diagonal octahedral chain of the galena-like slab. The N value can vary from 0 to 8, and possibly higher.[17] The combinations of these elements and selection of N can lead to dozens of ternary and quaternary pavonites.[18] Furthermore, the high stability of the structure allows the tuning of the band gap and property by suitable element selection.[18] Additionally, the pavonite compounds are semiconductors with metallic luster and are stable up to >800 K.[19,20] Recently, the thermoelectric properties of $AgBi_3S_5$ (pavonite with $N = 5$) were shown to be enhanced after doping with $BiCl_3$, and a ZT value close to unity was obtained.[21] This suggests that pavonites could be excellent thermoelectric materials, and are worthy of more detailed investigations.

Herein, we report the synthesis, crystal structure, and thermoelectric properties of two new quaternary chalcogenides $CdPbBi_4Se_8$ and $CdSnBi_4Se_8$ with the pavonite structure type. They are isostructural, crystallizing in the monoclinic space group $C2/m$. Pure phases of $CdPbBi_4Se_8$ and $CdSnBi_4Se_8$ were obtained by solid state synthesis, and both of them exhibit promising ZT values at high temperature.

■ EXPERIMENTAL SECTION

Reagents. All chemicals were used as obtained: cadmium metal (99.9%, Strem Chemicals, Inc.), bismuth metal (99.9%, Strem Chemicals, Inc.), lead metal (99.9%, Strem Chemicals, Inc.), selenium pellets (99.99%, American Elements, Inc.), tin metal (99.99%, Sigma-Aldrich, Inc.)

Synthesis. *$CdPbBi_4Se_8$.* Crystals of $CdPbBi_4Se_8$, large enough (>0.1 mm) for single crystal diffraction, were obtained by mixing Cd (83.9 mg, 0.75 mmol), Pb (113.3 mg, 0.55 mmol), Bi (334.4 mg, 1.60 mmol), and Se (294.8 mg, 3.73 mmol) with the starting ratio of Cd:Pb:Bi:Se = 1.65:1.17:3.4:8. The mixture was loaded into a 9 mm fused silica tube and flame-sealed at a vacuum of ∼10^{-4}, and then heated from room temperature (RT) to 350 °C in 6 h and held for 6 h for the complete melting of Se. This material was then heated to 750 °C in 12 h and held for 32 h, with slow cooling to 300 °C in 96 h and held for 1 h, followed by cooling to RT in 3 h. Pure phase was obtained by a slightly different method by using a stoichiometric starting material of Cd (449.6 mg 4.00 mmol), Pb (828.8 mg, 4.00 mmol), Bi (3343.6 mg, 16.00 mmol), and Se (2526.8 mg, 32.00 mmol) with molar ratio of Cd:Pb:Bi:Se = 1:1:4:8. The starting materials were combined together in a 13 mm fused silica tube in a dry, nitrogen-filled glovebox. The tube was evacuated to ∼10^{-4} mbar and flame-sealed. The tube was then placed in a programmable furnace. The mixtures were heated to 1000 °C and soaked there for 24 h, followed by water quenching to room temperature (RT). Subsequently, the sample was put into a programmable furnace and annealed at 550 °C for 8 days.

$CdSnBi_4Se_8$. $CdSnBi_4Se_8$ crystals were obtained by reacting a mixture of Cd (37.5 mg, 0.33 mmol), Sn (39.6 mg, 0.33 mmol), Bi (278.6 mg, 1.33 mmol), and Se (210.6 mg, 2.67 mmol) with a molar ratio of Cd:Sn:Bi:Se = 1:1:4:8. This mixture was heated from RT to 350 °C in 6 h and held for 6 h, and then it was heated to 780 °C in 12 h and held at this temperature for 32 h, with slow cooling to 300 °C in 96 h and followed by soaking at 300 °C for 1 h, and finally cooled to RT in 3 h. Good crystals with sizes larger than 0.1 mm were obtained. The pure phase of $CdSnBi_4Se_8$ was obtained by combining together Cd (215.7 mg, 1.92 mmol), Sn (231.6 mg, 1.95 mmol), Bi (1880.7 mg, 9.00 mmol), and Se (1374 mg, 17.40 mmol) with a molar ratio of Cd:Sn:Bi:Se = 0.88:0.90:4.14:8. The same method and heating profile used for $CdPbBi_4Se_8$ pure phase synthesis was used to obtain the $CdSnBi_4Se$ pure phase.

Powder X-ray Diffraction (PXRD). The purity of the synthesized samples was examined by Rigaku Miniflex powder X-ray diffractometer with Ni-filtered Cu Kα radiation operating at 40 kV and 15 mA. Mercury software was used to calculate PXRD spectra by using the CIFs of refined structures.

Scanning Electron Microscopy. Energy-dispersive X-ray spectroscopy (EDS) was conducted with a Hitachi S-3400 scanning electron microscope equipped with a PGT energy-dispersive X-ray analyzer. The EDS measurement was performed by using 25 kV accelerating voltage, 80 mA probe current, and 60 s acquisition time. The results reported here are an average of a large number of independent measurements.

Single Crystal X-ray Diffraction (SCXRD). X-ray diffraction measurements were conducted by using a STOE IPDS II single crystal diffractometer operating at 50 kV and 40 mA with Mo Kα radiation (λ = 0.71073 Å). Single crystals were picked up and adhered to the tip of glass fibers with glue. Data collections were carried out in X-Area software, and X-RED was used for the integration; X-SHAPE was used for numerical absorption corrections, and both X-RED and X-SHAPE are programs provided by STOE.[22] The crystal structures were solved by XPREP via direct methods and refined with the SHELXTL program package.[23]

The distinction of Bi and Pb or Sn and Cd atoms is not possible by X-ray diffraction.[17] Their relative proportion, according to EDS elemental analysis, is about $Cd_{1.0}Pb_{0.9}Bi_{3.9}Se_8$ and $Cd_{0.88}Sn_{0.90}Bi_{4.14}Se_8$, Figure S1. The crystal structure of $CdPbBi_4Se_8$ exhibits three distinct crystallographic Wyckoff sites 2*d*, 4*i*, 2*a*. The refinement of the crystal structure was indistinct due to the very similar X-ray scattering power of lead (Z = 82) and bismuth (Z = 83). According to the refinement, two 4*i* sites and one 2*d* site can be assigned to Bi or Pb. The 2*d* site was denoted to be Pb, and two 4*i* sites were assigned as Bi which is in accordance with the EDS results of the crystal used for SCXRD, which gave a ratio for Pb:Bi of ∼1:4. With the 2*a* site solely occupied by Cd, we obtained an R_1 of 4.12%. By using mixed occupancy of the Cd site by Pb or Bi the R_1 lowered to 3.76%. The Pb at the 2*d* site mixed with Cd further lowered R_1 to 3.69% and gave a Cd occupancy of 0.084%. By mixing the Bi2 (4*i*) with Cd the R_1 value slightly dropped to 3.67% and gave a Cd occupancy of 0.035% with a final composition of $Bi_{4.1}Cd_1Pb_{0.9}Se_8$. The Bi1 (4*i*) site did not accept any Cd giving a negative occupancy for it. The charge balanced composition of $CdPbBi_4Se_8$ was obtained with a final R_1 value of 3.99%.

A similar behavior was observed with $CdSnBi_4Se_8$, in this case compounded by the very similar X-ray scattering power of cadmium (Z = 48) and tin (Z = 50). Assigning the 2*a* site to Cd gave an R_1 of 3.16% compared with an R_1 of 3.10% when assigning the 2*a* site to Sn. Therefore, Sn was assigned to occupy the 2*a* site. According to EDS analysis ($Cd_{0.88}Sn_{0.9}Bi_{4.14}Se_8$), the Bi sites are refined to be mix occupied with Cd. Finally, a composition of $SnCd_{0.9}Bi_{4.15}Se_8$ was obtained which is very close to the charge balanced formula of $CdSnBi_4Se_8$, and a final R factor of 3.12%. The crystal data and structure refinement results are listed in Table 1, and selected bond lengths of $CdPbBi_4Se_8$ and $CdSnBi_4Se_8$ are in Table 2. Atomic coordinates, equivalent isotropic displacement parameters, and anisotropic displacement parameters of $CdPbBi_4Se_8$ and $CdSnBi_4Se_8$ are given in Tables S1−S4.

Thermal Analysis. About 75 mg of $CdPbBi_4Se_8$ and 60 mg of $CdSnBi_4Se_8$ powder samples were placed into two fused silica ampules, and then flame-sealed at a vacuum of $\sim 10^{-4}$ mbar. Differential thermal analysis (DTA) measurements were conducted on a Shimadzu DTA-50 thermal analyzer using a temperature rate of ±10 °C/min and a maximum temperature of 1000 °C for two cycles. Melting and crystallization temperatures were identified at the minimum of endothermic valleys and the maximum of exothermic peaks. The DTA products were collected and examined with PXRD after the experiments.

Spark Plasma Sintering (SPS). The obtained $CdPbBi_4Se_8$ and $CdSnBi_4Se_8$ ingots were crushed into fine powders and subsequently densified at 773 K, for 10 min in a 12.7 mm diameter graphite die under an axial compressive stress of 40 MPa using SPS method (SPS-211LX, Fuji Electronic Industrial Co., Ltd.). A highly dense disc-shaped pellet with ∼92% of its theoretical density was obtained.

Electrical Properties. The SPS-processed pellets of $CdPbBi_4Se_8$ and $CdSnBi_4Se_8$ were cut into bars both perpendicular and parallel to the sintering pressure directions. The samples were spray-coated with boron nitride to minimize outgassing, except in places needed for electrical contact with the thermocouples, heater, and voltage probes. The Seebeck coefficients and electrical conductivities were measured both perpendicular and parallel to the sintering pressure directions with an Ulvac Riko ZEM-3 instrument simultaneously under a low-pressure helium atmosphere with a temperature ranging from room temperature to 850 K. The uncertainty of the measured Seebeck coefficient and electrical conductivity is about 5%.[24]

Table 2. Bond Lengths [Å] for $CdPbBi_4Se_8$ and $CdSnBi_4Se_8$ at 293(2) K with Estimated Standard Deviations in Parentheses[a]

$CdPbBi_4Se_8$	distances	$CdSnBi_4Se_8$	distances
Pb(1)−Se(1)	2.9206(12)	Bi(1)−Se(1)	2.9199(8)
Pb(1)−Se(2)	2.9210(18)	Bi(1)−Se(3)	2.9312(11)
Bi(2)−Se(1)	3.0855(13)	Bi(2)−Se(1)	2.9990(13)
Bi(2)−Se(1)#4	3.0855(13)	Bi(2)−Se(1)#4	3.0674(9)
Bi(2)−Se(1)#5	2.9946(19)	Bi(2)−Se(1)#5	3.0674(9)
Bi(2)−Se(2)	2.8363(12)	Bi(2)−Se(3)	2.8281(9)
Bi(2)−Se(3)	2.9234(19)	Bi(2)−Se(4)	2.9038(13)
Bi(1)−Se(3)	2.8669(13)	Bi(3)−Se(2)	3.1001(9)
Bi(1)−Se(4)	2.747(2)	Bi(3)−Se(2)	2.7093(13)
Bi(1)−Se(4)	3.1219(13)	Bi(3)−Se(4)	2.8545(10)
Cd(3)−Se(3)	2.707(2)	Sn(1)−Se(2)	2.9125(8)
Cd(3)−Se(4)	2.9189(11)	Sn(1)−Se(4)	2.6798(13)

[a] Symmetry transformations used to generate equivalent atoms: $x, y + 1, z$; (2) $-x, -y + 1, -z + 1$; (3) $-x, -y, -z + 1$; (4) $x, y - 1, z$; (5) $-x - {}^1/_2, -y - {}^1/_2, -z + 1$; (6) $x - {}^1/_2, y - {}^1/_2, z$; (7) $x - {}^1/_2, y - {}^3/_2, z$; (8) $-x - {}^1/_2, -y - {}^3/_2, -z$; (9) $-x - {}^1/_2, -y - {}^5/_2, -z$; (10) $-x - 1, -y - 1, -z$; (11) $-x - 1, -y - 2, -z$; (12) $x + {}^1/_2, y + {}^1/_2, z$; (13) $x + {}^1/_2, y + {}^3/_2, z$.

Thermal Conductivity. The thermal diffusivity coefficient (D) measurements were conducted with the samples cut from the same pellet processed by SPS. The thermal diffusion both perpendicular and parallel to the sintering pressure directions is measured by using a Netzsch LFA457 instrument. The samples were coated with graphite to minimize errors from the emissivity of the material. The Cowan model with pulse correction was used for the thermal diffusivity data analysis. The total thermal conductivity was calculated with the $\kappa_{tot} = DC_pd$ equation, where d is the actual density calculated by using the mass and the volume of the sample. The specific heat capacity (C_p) was calculated by the Dulong−Petit law $C_p = 3R/\bar{M}$, where R is the gas constant 8.314 J mol^{-1} K^{-1} and $\bar{M}$ is the average molar mass of $CdPbBi_4Se_8$ and $CdSnBi_4Se_8$, respectively. Thermal conductivity (κ_{total}) is composed of electrical thermal conductivity (κ_{ele}) and lattice thermal conductivity (κ_{lat}). κ_{ele} can be estimated by the Wiedemann−Franz law $\kappa_{ele} = L\sigma T$. In the equation, L is the Lorenz number which is temperature dependent and was calculated using the measured Seebeck coefficients;[25] σ is electrical conductivity, and T is temperature. The lattice thermal conductivity can be obtained by subtracting κ_{ele} from κ_{total}. The uncertainty of the thermal conductivity is estimated to be within 8%, and the uncertainty is 12% for ZT.[24]

Hall Measurement. The carrier concentrations were obtained via Hall effect measurements on samples of these compounds using a Quantum Design PPMS at room temperature. Contacts were made with gold wires attached to the sample surface using Dupont 4929N silver paste. The Hall resistivity $R_{xy} = [R(+H) - R(-H)]/2$ was obtained by switching the magnetic field at each point to reduce the effect of Hall electrode misalignment.

Density Functional Theory (DFT) Calculations. The total energies and relaxed geometries were calculated by DFT within the generalized gradient approximation (GGA) of the Perdew−Burke−Ernzerhof for exchange correlation functional with projector augmented wave potentials.[26] We use periodic boundary conditions and a plane wave basis set as implemented in the Vienna ab initio simulation package.[27] The total energies were numerically converged to approximately 3 meV/cation using a basis set energy cutoff of 500 eV and dense k-meshes corresponding to 4000 k-points per reciprocal atom in the Brillouin zone.

DOI: 10.1021/acs.chemmater.7b03328
Chem. Mater. 2017, 29, 8494−8503

Phonon Dispersion Calculations. To quantitatively explore the origin of lattice thermal conductivity at the atomic level, we utilize the Debye−Callaway model to quantitatively evaluate the value of lattice thermal conductivity of $CdSnBi_4Se_8$. It is known that the Grüneisen parameters, which characterize the relationship between phonon frequency and crystal volume change, are useful to estimate the lattice anharmonicity and are thus helpful to interpret the physical nature of lattice thermal conductivity behavior.[28,29] The phonon and Grüneisen dispersions are calculated using first-principles DFT phonon calculations within the quasiharmonic approximation. The $CdSnBi_4Se_8$ phonon dispersions are calculated on a 126 atom supercell at two volumes: one is the equilibrium volume V_0, and another one is the isotropically compressed volume $0.98V_0$.

The Debye−Callaway formalism[30−32] has recently been shown to produce accurate values of lattice thermal conductivity, compared to experiment, for low-conductivity thermoelectric compounds.[28,33] The total lattice thermal conductivity can be written as a sum over one longitudinal κ_{LA} and two transverse κ_{TA} and κ'_{TA} acoustic phonon branches: $\kappa_{Latt} = \kappa_{LA} + \kappa_{TA} + \kappa'_{TA}$. The partial conductivities κ_i (i corresponds to TA, TA′, and LA modes) are given by

$$\kappa_i = \frac{1}{3}C_iT^3\left\{\int_0^{\theta_i/\mathrm{T}} \frac{\tau_c^i(x)x^4e^x}{(e^x-1)^2}dx + \frac{\left[\int_0^{\Theta_i/T}\frac{\tau_c^i(x)x^4e^x}{\tau_N^i(e^x-1)^2}dx\right]^2}{\int_0^{\Theta_i/T}\frac{\tau_c^i(x)x^4e^x}{\tau_N^i\tau_U^i(e^x-1)^2}dx}\right\} \tag{1}$$

In this expression, Θ_i is the longitudinal (transverse) Debye temperature, $1/\tau_N^i$ is the scattering rate for normal phonon processes, $1/\tau_R^i$ is the sum of all resistive scattering processes, and $1/\tau_c^i = 1/\ \tau_N^i + 1/\tau_R^i$, $x = \hbar\omega/k_BT$, and $C_i = k_B^4/2\pi^2\hbar^3v_i$. Here, $\hbar$ is the Planck constant, k_B is the Boltzmann constant, ω is the phonon frequency, and v_i is the longitudinal or transverse acoustic phonon velocity.

The resistance scattering rate is the sum of scattering rates due to Umklapp phonon−phonon scattering ($1/\tau_U^i$), mass-difference impurity scattering ($1/\tau_m^i$), boundary scattering ($1/\tau_B^i$), and electron−phonon scattering ($1/\tau_{e-ph}^i$). In the pure single crystal compounds considered here, we ignore the effect of impurity scattering, and we assume that boundary and electron−phonon scattering contributions can be ignored at temperatures above approximately 100 K. Thus, the resistive scattering rate is mainly determined by the Umklapp phonon−phonon processes ($1/\tau_r^i \cong 1/\tau_U^i$). The normal phonon scattering and Umklapp can be written as

$$\frac{1}{\tau_N^{LA}(x)} = \frac{k_B^5\gamma_{LA}^2V}{M\hbar^4v_{LA}^5}x^2T^5 \tag{2}$$

$$\frac{1}{\tau_N^{TA/TA'}(x)} = \frac{k_B^5\gamma_{TA/TA'}^2V}{M\hbar^4v_{TA/TA'}^5}xT^5 \tag{3}$$

$$\frac{1}{\tau_U^i(x)} = \frac{k_B^2\gamma_i^2}{M\hbar v_i^2\Theta_i}x^2T^3e^{-\theta_i/3T} \tag{4}$$

where γ, V, and M are the Gruneisen parameter, the volume per atom, and the average mass of an atom in the crystal, respectively. The Grüneisen parameter can be defined as $\gamma_i = -\frac{V\partial\omega_i}{\omega_i\partial V}$, characterizing the relationship between phonon frequency and volume change.

RESULTS AND DISCUSSION

Synthesis and Thermal Behavior. Single crystals with edge length up to 0.1 mm, suitable for X-ray diffraction, were obtained by heating the mixture of the starting materials to 750 °C in a vacuum-sealed tube with a slow cooling rate of ∼4.7 °C/h. The pure phase of $CdPbBi_4Se_8$ was synthesized by heating a stoichiometric ratio mixture of Cd, Pb, Bi, and Se in a vacuum-sealed fused silica tube to 1000 °C and water quench, followed by annealing the ingot at 550 °C for 8 days. For the $CdSnBi_4Se_8$ analogue, pure phase was obtained by the same method with the starting materials slightly off the stoichiometric ratio, Cd:Sn:Bi:Se = 0.88:0.90:4.14:8. Black solid ingots were obtained, and the phase purities were validated by comparison of the PXRD of synthesized and simulated patterns, Figure 1. Both $CdPbBi_4Se_8$ and $CdSnBi_4Se_8$ are air stable and insoluble in water, ethanol, or acetone.

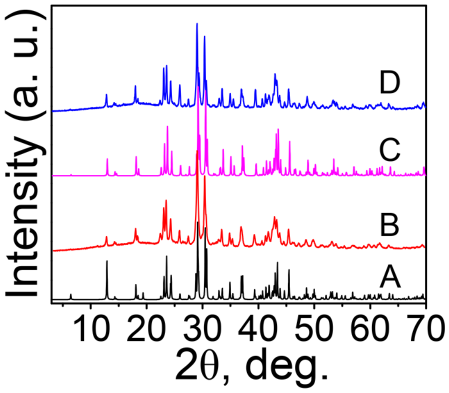

Figure 1. Experimental powder X-ray diffraction patterns (PXRD) in comparison to simulated ones: (A) $CdPbBi_4Se_8$ simulated, (B) $CdPbBi_4Se_8$ synthesized, (C) $CdSnBi_4Se_8$ simulated, (D) $CdSnBi_4Se_8$ synthesized.

DTA was used to understand the thermal behavior of $CdPbBi_4Se_8$ and $CdSnBi_4Se_8$ from room temperature (RT) to 1000 °C (Figure 2). $CdPbBi_4Se_8$ revealed two endothermic peaks at 701 and 734 °C on heating. The peak at 701 °C can be attributed to the phase decomposition which was further confirmed by PXRD of the DTA product. The endothermic peak at 734 °C corresponds to the melting of $CdPbBi_4Se_8$ which is not totally decomposed. On cooling, there are two exothermic peaks corresponding to the crystallization of the decomposed compound and residual $CdPbBi_4Se_8$ at 698 and

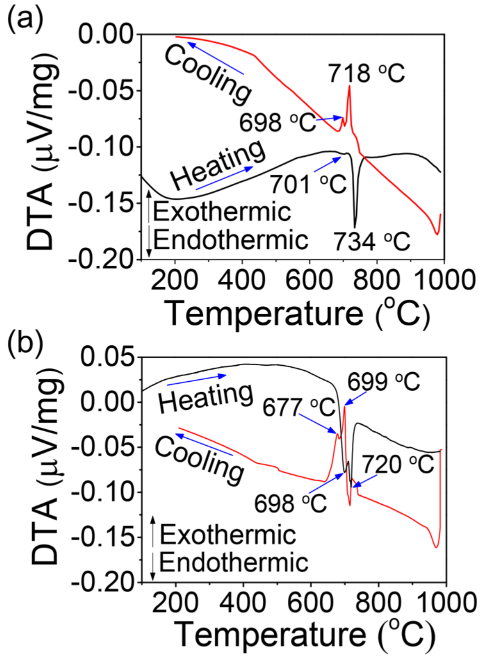

Figure 2. DTA curves of (a) $CdPbBi_4Se_8$ and (b) $CdSnBi_4Se_8$.

718 °C, respectively. These results remain consistent over two DTA cycles, Figure S2. PXRD measurement was performed on the DTA product afterward; some of the peaks match the PXRD of the sample before heating, while some peaks cannot be indexed, which means the compound decomposed to unknown phases at high temperature, as shown in Figure S3. The DTA experiment for $CdSnBi_4Se_8$ revealed two endothermic peaks at 698 and 720 °C which correspond to the decomposition and melting of $CdSnBi_4Se_8$, respectively. On cooling there are two peaks at 677 and 699 °C which correspond to the crystallization of the decomposed product and the residual $CdSnBi_4Se_8$, respectively. PXRD of the DTA product also confirms the incongruent melting behavior of $CdSnBi_4Se_8$, Figure S2.

Crystal Structure. $CdPbBi_4Se_8$ and $CdSnBi_4Se_8$ are isostructural, and both of them crystallize in the monoclinic system with the *C*2/*m* space group. Figure 3 depicts the unit cell contents of $CdPbBi_4Se_8$ and $CdSnBi_4Se_8$. The cation coordination environments of $CdPbBi_4Se_8$ are shown in Figure 4. The Bi1 site is solely occupied by Bi, and it coordinates with 5 Se atoms forming a squared pyramid with Bi1−Se bond distances ranging from 2.747(2) to 3.1219(13) Å. These bond distances are similar to those reported in $Rb_2CdBi_6Se_{11}$[34] and $Pb_6Bi_2Se_9$.[35] There are another two Se atoms which are 3.557 Å away from Bi1 that are too far to be considered bonded, see Figure 4. Both Bi/Cd2 and Bi/Cd3 sites are surrounded by six Se atoms forming distorted octahedra. The Bi/Cd−Se bond distances range from 2.707(2) to 3.0855(13) Å which is comparable to those in $Cs_{1.13}Cd_{1.13}Bi_{2.87}Se_6$.[36] Pb/Cd1 is coordinated to six Se atoms forming a regular octahedra with Pb/Cd1−Se bond distance of 2.9206(12) Å.

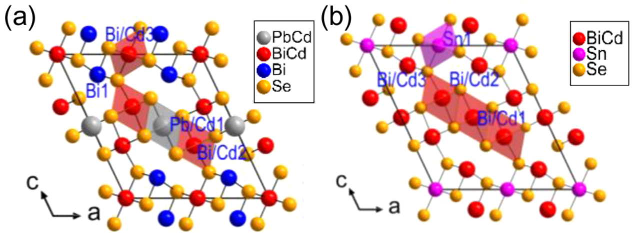

Figure 3. Ball-and-stick representation of the unit cell viewed along the *b*-axis of (a) $CdPbBi_4Se_8$ and (b) $CdSnBi_4Se_8$.

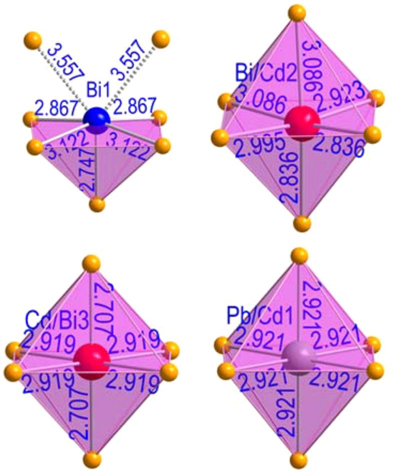

Figure 4. Coordination environments of Bi, Bi/Cd, Pb/Cd (the orange balls represent Se atoms) in $CdPbBi_4Se_8$, labeling with the nearest bond distances.

$CdPbBi_4Se_8$ possesses a pavonite structure which consists of two types of slabs that we denote as thin and thick slabs.[2] The slabs can be described as an assembly of blocks excised from the cubic NaCl lattice perpendicular to the [311] direction.[37,38] Figure 5a shows the typical pavonite structure of $AgBi_3S_5$ for comparison, while Figure 5b shows the composed slabs of $CdPbBi_4Se_8$. The thin slab (Slab I) of $CdPbBi_4Se_8$ is one octahedron wide and contains one octahedron $[(Bi/Cd)3Se_6]$ and a pair of squared pyramids $[Bi1Se_5]$. This is similar to Slab I in $AgBi_3S_5$. The thick slab (Slab II) of $CdPbBi_4Se_8$ is made of a distorted galena-type (or NaCl-type) lattices with one $[(Pb/Cd)1Se_6]$ and two $[(Bi/Cd)2Se_6]$ octahedron per one diagonal octahedral chain. By comparison, the Slab II in $AgBi_3S_5$ is composed of four $[BiS_6]$ and one $[AgS_6]$ octahedron along the diagonal octahedral chain. According to the general chemical formula of $M_{N+1}Bi_2Q_{N+5}$, $CdPbBi_4Se_8$ has N equal to 3 and $AgBi_3S_5$ has N equal to 5. In $CdPbBi_4Se_8$, these three octahedra wide fragments are reconnected to build the step-shaped layers which extend over the *ab*-plane. The two slabs are interconnected with each other through sharing a Se3 atom. This layered modular construction gives the compound both an anisotropic morphology and electronic structure.

Band Structure Calculations. In order to understand the nature of the electronic structure in $CdPbBi_4Se_8$ and $CdSnBi_4Se_8$, band structure calculations were performed. Figure 6 shows that the band structures of $CdSnBi_4Se_8$ and $CdPbBi_4Se_8$ are very similar.

The two band structures are qualitatively quite similar, with the main difference being the lower band gap of $CdSnBi_4Se_8$ (∼0.16 eV) compared to that of $CdPbBi_4Se_8$ (∼0.42 eV). This is consistent with other isostructural examples of Sn and Pb analogues such as SnTe[39,40] and PbTe,[41,42] and $CsSnBr_3$[43] and $CsPbBr_3$.[44] Moreover, the electronic density of states decomposition shows that the valence bands within −0.75 to 0 eV of the VBM for $CdSnBi_4Se_8$ are mainly due to the hybridization of Sn 5s and Se 4p electrons. Similarly, in $CdPbBi_4Se_8$, the top valence bands are from the hybridization of Pb 6s and Se 4p electrons. The presence of either Sn or Pb in these compounds controls the position of the valence band states and thus induces different band gaps.

Thermoelectric Properties. The dense $CdPbBi_4Se_8$ and $CdSnBi_4Se_8$ pellets prepared by the spark plasma sintering (SPS) technique exhibit anisotropy that derives from the anisotropic structure and morphology of the materials. Preferred orientation of the crystallites may occur when it is subjected to high pressure from SPS sintering. Thus, the Seebeck coefficient, electrical conductivity, and thermal conductivity were measured along both directions perpendicular and parallel to the SPS pressure. Figure 7a,b shows the cutting scheme for the samples and the pictures of the resulting specimens of $CdPbBi_4Se_8$ which were used for the measurements. Figure 7c,d shows SEM images of the freshly fractured surfaces of $CdPbBi_4Se_8$ and $CdSnBi_4Se_8$ specimens. The images show that the samples were fully dense without noticeable cracks or pores. The EDS mapping of the imaged area demonstrates that all the elements are homogeneously dispersed in both $CdPbBi_4Se_8$ and $CdSnBi_4Se_8$. Figure S4 shows the X-ray diffraction patterns of samples cut along directions parallel and perpendicular to the SPS pressure direction. For both $CdPbBi_4Se_8$ and $CdSnBi_4Se_8$, a slightly

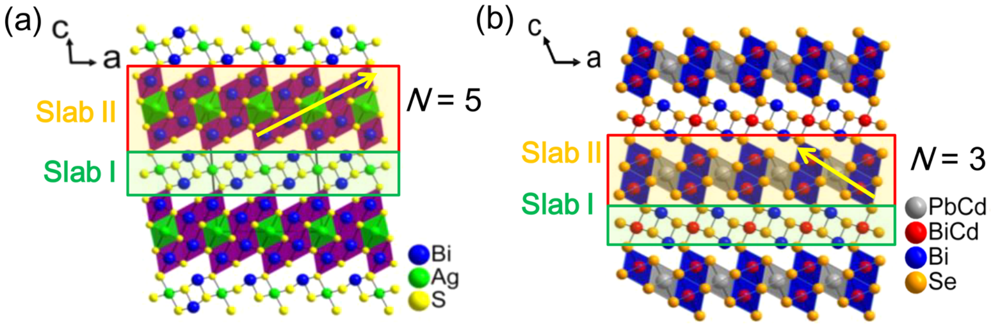

Figure 5. Structure comparison between two different members of the pavonite family that illustrate the common building block and the varying building block (a) $AgBi_3S_5$ and (b) $CdPbBi_4Se_8$; the arrows in the figure show the octahedron chain in the varying galena-type layer.

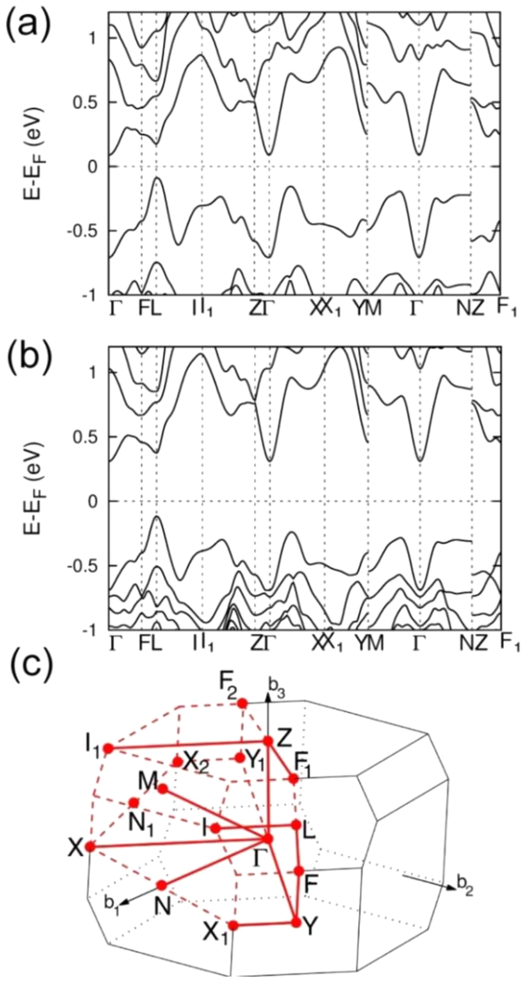

Figure 6. (a) Electronic band structure of $CdSnBi_4Se_8$, (b) electronic band structure of $CdPbBi_4Se_8$, and (c) the Brillouin zone. $CdSnBi_4Se_8$ and $CdPbBi_4Se_8$ show an indirect band gap of 0.16 and 0.42 eV, respectively.

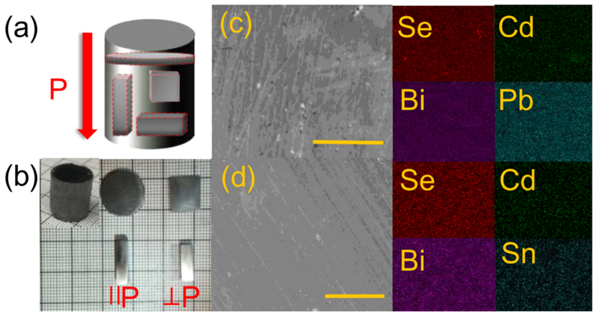

Figure 7. (a) Samples cutting motif and pressure directions in the pellet processed by SPS; (b) the cut specimens used for measurements (perpendicular or parallel means the direction of SPS pressure); (c) freshly fractured surface of $CdPbBi_4Se_8$ sample processed by SPS and characterized by scanning electron microscope (SEM) and energy-dispersive X-ray spectroscopy; (d) freshly fractured surface of $CdSnBi_4Se_8$ SPS-processed sample characterized by SEM and energy-dispersive X-ray spectroscopy. The scale bar is 100 μm.

preferred orientation was observed. All measurements were performed to no higher than 850 K to avoid any possible phase decomposition, and all the data from these measurements were reversible upon ramping and cooling, Figure S5.

The electrical conductivities of the SPS-processed $CdPbBi_4Se_8$ and $CdSnBi_4Se_8$ samples show anisotropic behavior, Figure 8a, which arises from the preferential orientation of the crystallites. Along the direction perpendicular to the SPS pressure, $CdPbBi_4Se_8$ features an electrical conductivity of 78 S cm^{-1} at 320 K. It decreases with increasing temperature and reaches the minimum value of 42 S cm^{-1} at 673 K, and then increases slightly to 50 S cm^{-1} at 840 K due to bipolar conduction. The electrical conductivity parallel to the SPS pressure direction has the same temperature dependence, but the absolute value is lower. Specifically, the highest and lowest values are 43 S cm^{-1} at 320 K and 27 S cm^{-1} at 673 K, respectively. Hall measurements show that the carrier concentration of $CdPbBi_4Se_8$ is 3.21×10^{19} cm^{-3} at RT. The measured magnetic-field dependence of Hall resistivity ρ_{xy} is shown in Figure S7. This corresponds to an electron mobility of 15.2 cm^2 V^{-1} s^{-1}. The electrical conductivity values of $CdPbBi_4Se_8$ are comparable to that of the reported pavonites, e.g., $Mn_{1.34}Sn_{6.66}Bi_8Se_{20}$ (with $N = 5$)[19] and $InSn_2Bi_3Se_8$ (with $N = 3$) with conductivities of 47 and 78.59 S cm^{-1} at RT, respectively.[20] The electrical conductivity of $CdSnBi_4Se_8$ is much higher than that of $CdPbBi_4Se_8$. In the direction perpendicular to the SPS pressure, $CdSnBi_4Se_8$ possesses a conductivity of 150 S cm^{-1} at 320 K, and it decreases with increasing temperature, reaching the lowest value of 106 S cm^{-1} at 650 K. Then, it slightly increases to 133 S cm^{-1} at 850 K. In the direction parallel to the SPS pressure, the same temperature dependence was observed, but the values are lowered by nearly one-third. Hall measurements at room temperature for a $CdSnBi_4Se_8$ pristine sample reflect a carrier concentration of 2.85×10^{19} cm^{-3} and an electron mobility of 32.9 cm^2 V^{-1} s^{-1}.

The Seebeck coefficients of $CdPbBi_4Se_8$ and $CdSnBi_4Se_8$ show negligible anisotropy, Figure 8b. At 320 K, the Seebeck

DOI: 10.1021/acs.chemmater.7b03328
Chem. Mater. 2017, 29, 8494−8503

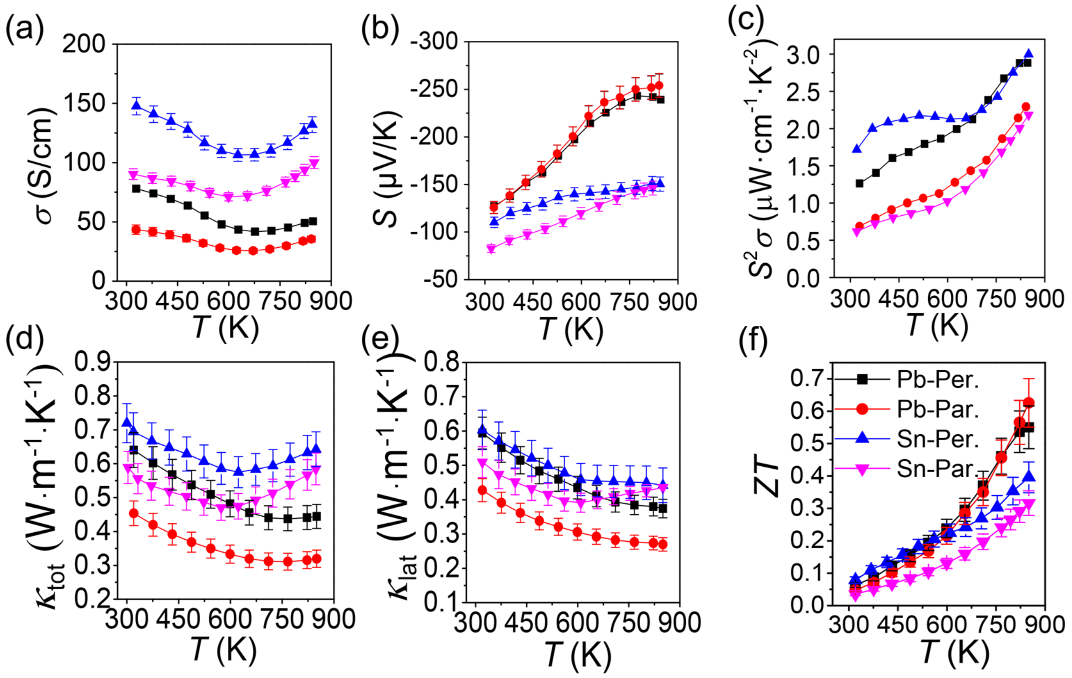

Figure 8. (a) Electrical conductivity, (b) Seebeck coefficient, (c) power factor, (d) total thermal conductivity, (e) lattice thermal conductivity, and (f) figure of merit as a function of temperature. Pb-Per. and Pb-Par. denote the properties of $CdPbBi_4Se_8$ measured perpendicular and parallel to the SPS pressure direction, respectively. Sn-Per. and Sn-Per. denote the properties of $CdSnBi_4Se_8$ measured perpendicular and parallel to the SPS pressure direction, respectively.

value of $CdPbBi_4Se_8$ is about -127 μV K^{-1}, indicating n-type conduction, and reaches -254 μV K^{-1} at 850 K. The Seebeck coefficient of $CdSnBi_4Se_8$ has the same temperature dependence as $CdPbBi_4Se_8$. Along the measurement direction perpendicular to the SPS pressure, $CdSnBi_4Se_8$ shows Seebeck coefficient values of -107 μV K^{-1} at 320 K and -150 μV K^{-1} at 850 K. The Seebeck coefficient of $CdSnBi_4Se_8$ is -83 μV K^{-1} at 320 K along the measurement direction parallel to the SPS pressure. The high-temperature Seebeck coefficients are equal along two directions.

The power factors (PF = $S^2\sigma$) as a function of temperature are shown in Figure 8c. Power factor values of 2.9 μW cm^{-1} K^{-2} and 3.0 μW cm^{-1} K^{-2} were obtained for $CdPbBi_4Se_8$ and $CdSnBi_4Se_8$ at 850 K, respectively. These values are comparable to that of $CsAg_5Te_3$ (~3.9 μW cm^{-1} K^{-2} at 727 K)[45] and higher than that of undoped $AgBi_3S_5$ (~1.5 μW cm^{-1} K^{-2} at 750 K).[21]

Similar to electrical conductivity, the thermal conductivity also has very strong directional dependence. The thermal conductivity of $CdPbBi_4Se_8$ decreases with increasing temperature. Along the direction perpendicular to the SPS pressure, the highest value of 0.64 W m^{-1} K^{-1} was observed at 320 K, and between 710 and 850 K it reaches the minimum of ~0.44 W m^{-1} K^{-1}. The thermal conductivity along the direction parallel to the SPS pressure is even lower with values of 0.45 W m^{-1} K^{-1} 320 K and 0.32 W m^{-1} K^{-1} at 850 K. These values are comparable with those of SnSe.[28] The thermal conductivity is also comparable to that of $AgBi_3S_5$ which exhibits ~0.6 W m^{-1} K^{-1} at room temperature and 0.45 W m^{-1} K^{-1} at ~700 K.[21] For $CdSnBi_4Se_8$, along the direction perpendicular to the SPS pressure, the thermal conductivity is 0.69 W m^{-1} K^{-1} at 320 K. It decreases with rising temperature with the lowest value of 0.58 W m^{-1} K^{-1} at 620 K. Along the direction parallel to pressure, it lowers to 0.57 W m^{-1} K^{-1} at 320 K and 0.47 W m^{-1} K^{-1} at 620 K. The lattice thermal conductivities of both $CdPbBi_4Se_8$ and $CdSnBi_4Se_8$ were calculated using the Wiedemann–Franz relation, Figure 8e, and the relationship between Lorenz number and temperature is given in Figure S8. In the direction perpendicular with the SPS pressure, $CdPbBi_4Se_8$ has the highest κ_{lat} value of 0.59 W m^{-1} K^{-1} at 320 K, and it decreases with rising temperatures with the lowest value of 0.37 W m^{-1} K^{-1} at 850 K. In the direction parallel to the pressure the κ_{lat} is even lower with 0.43 W m^{-1} K^{-1} at 320 K and decreases with rising temperature, achieving the lowest value of 0.27 W m^{-1} K^{-1} at 850 K. $CdSnBi_4Se_8$ possesses a κ_{lat} of 0.60 W m^{-1} K^{-1} at 320 K and 0.44 W m^{-1} K^{-1} at 850 K along the direction perpendicular to the SPS pressure. Comparably, along the direction parallel to the SPS pressure κ_{lat} of 0.51 W m^{-1} K^{-1} and 0.44 W m^{-1} K^{-1} at 320 and 850 K were obtained, respectively. For both $CdPbBi_4Se_8$ and $CdSnBi_4Se_8$, κ_{lat} values measured in the direction parallel to the SPS pressure are lower than that in the direction perpendicular to the SPS pressure. The negative temperature dependence of κ_{lat} for both $CdPbBi_4Se_8$ and $CdSnBi_4Se_8$ is due to the enhanced Umklapp phonon scattering with increasing temperature. Thus, the κ_{total} decreases with rising temperature, and this trend is also observed in doped PbTe[46] and SnSe.[9,28]

On the basis of the above measured transport properties, the ZT values of $CdPbBi_4Se_8$ and $CdSnBi_4Se_8$ were calculated, Figure 8f. The ZT values for $CdPbBi_4Se_8$ and $CdSnBi_4Se_8$ are almost unaffected by the measuring directions. The highest ZT values of 0.63 and 0.40 were obtained for $CdPbBi_4Se_8$ and $CdSnBi_4Se_8$ at 850 K, respectively. These values are higher than that for pristine $AgBi_3S_5$ which has the highest ZT value of ~0.22 at 750 K. The highest ZT value of $CdPbBi_4Se_8$ is slightly lower than the maximum ZT value of pristine PbTe which was reported between 0.8 and 1.0 at approximately 650 K[47] and 0.8 at 700 K.[48] Our results suggest that both $CdPbBi_4Se_8$ and

DOI: 10.1021/acs.chemmater.7b03328
Chem. Mater. 2017, 29, 8494–8503

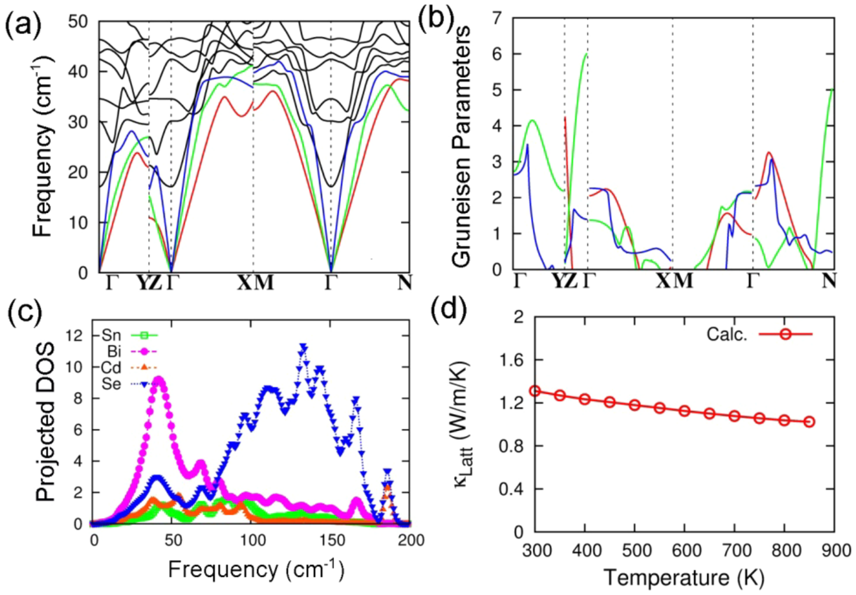

Figure 9. (a) Phonon and (b) Grüneisen dispersions for $CdSnBi_4Se_8$. (c) The projected phonon density of states for $CdSnBi_4Se_8$. (d) The temperature dependent lattice thermal conductivities of $CdSnBi_4Se_8$, calculated by the Debye−Callaway model.

$CdSnBi_4Se_8$ are good candidate materials for enhancement of ZT via doping, band gap engineering, and nanostructuring. Figure S6 shows that by doping 0.2% Br (with 0.1% $PbBr_2$) the conductivity of $CdPbBi_4Se_8$ can be boosted from 78 to 161 S cm^{-1} at 320 K but the Seebeck lowered due to the increased carrier concentration. The carrier concentration of the 0.2% Br doped $CdPbBi_4Se_8$ sample was 5.06×10^{19} cm^{-3} at RT and the electron mobility ~20 cm^2 V^{-1} s^{-1}. Finally, the power factor increased from 2.9 to 3.4 μW cm^{-1} K^{-2} at 850 K. This doping experiment demonstrates that further improvements of ZT values are expected via systematic doping studies to control the concentration of carriers.

In order to obtain further insight into the origin of the low lattice thermal conductivity of $CdSnBi_4Se_8$ we carried out phonon dispersion and Grüneisen dispersion calculations, Figure 9a,b. To quantitatively evaluate the anharmonicity along these directions, we plot the dispersion of the Grüneisen parameters of acoustic modes in $CdSnBi_4Se_8$, Figure 9b. We further calculated the average Grüneisen parameter (γ) of each acoustic dispersion. The average acoustic Grüneisen parameters are, respectively, $\gamma_{TA} = 1.82$, $\gamma_{TA'} = 2.1$, $\gamma_{LA} = 1.45$. These values are smaller than the average Grüneisen parameters of SnSe γ = 4.1, a remarkable material that demonstrates a strong anharmonicity and possesses ultralow lattice thermal conductivity.[28,49] On the basis of the phonon dispersions and Grüneisen parameters, we calculated the lattice thermal conductivities of $CdSnBi_4Se_8$, as shown in Figure 9d. The calculated value is about 1.3 W m^{-1} K^{-1} at 300 K, which is somewhat larger than the measurements of lattice thermal conductivity around 0.58 W m^{-1} K^{-1}. This is reasonable since the extra phonon scattering induced by Cd, Sn, and Bi disordering (mixed occupied sites in the structure) is not considered in our calculations. In Figure 9c, the projected phonon density of states indicates that the low-frequency modes are mainly contributed from Bi atom vibrations similar to those discussed in $AgBi_3S_5$.[21]

CONCLUDING REMARKS

We report two new isostructural pavonites $CdPbBi_4Se_8$ and $CdSnBi_4Se_8$, which form as doped n-type semiconductors. The compounds are robust and have good thermal and mechanical stabilities. DFT calculations indicate that they are indirect band gap semiconductors. The complex composition and the anisotropic structure of these materials yield an extremely low thermal conductivity of <0.69 W m^{-1} K^{-1}. $CdPbBi_4Se_8$ and $CdSnBi_4Se_8$ pristine samples show maximum ZT values of ~0.63 and ~0.40 at 850 K, respectively. The pavonite chalcogenides may represent a new promising family for thermoelectric candidate materials.

ASSOCIATED CONTENT

Supporting Information

The Supporting Information is available free of charge on the ACS Publications website at DOI: 10.1021/acs.chemmater.7b03328.

Tables of atomic coordinates and displacement parameters of $CdPbBi_4Se_8$ and $CdSnBi_4Se_8$, SEM image and energy-dispersive X-ray spectroscopy spectrum, and PXRD after DTA (PDF)

X-ray crystallographic data for $CdPbBi_4Se_8$ (CIF)

X-ray crystallographic data for $CdSnBi_4Se_8$ (CIF)

AUTHOR INFORMATION

Corresponding Author

*E-mail: m-kanatzidis@northwestern.edu.

ORCID

Jing Zhao: 0000-0002-8000-5973
Gangjian Tan: 0000-0002-9087-4048
Xianli Su: 0000-0003-4428-6461
Haijie Chen: 0000-0003-3567-1763
Wenwen Lin: 0000-0002-1627-9558
Chris Wolverton: 0000-0003-2248-474X
Mercouri G. Kanatzidis: 0000-0003-2037-4168

Author Contributions

All authors have given approval to the final version of the manuscript.

Notes

The authors declare no competing financial interest.

■ ACKNOWLEDGMENTS

This work was supported in part by the National Science Foundation (Grant DMR-1708254, exploratory synthesis of pavonites) and in part by by the U.S. Department of Energy, Office of Science, and Office of Basic Energy Sciences under Award Number DE-SC0014520 (electronic structure calculations, sample measurements, thermoelectric characterization). This work made use of the EPIC facility (NUANCE Center-Northwestern University), which has received support under the State of Illinois, Northwestern University, and the National Science Foundation with Grants DMR-1121262 through the MRSEC program at the Materials Research Center, and EEC-0118025/003 through The Nanoscale Science and Engineering Center. S.H. and C.W. (DFT calculations) acknowledge support from the Department of Energy, Office of Science Basic Energy Sciences under Grant DE-SC0014520. This work was supported in part by a grant from the National Science Foundation of China (51702329).

■ REFERENCES

(1) Snyder, G. J.; Toberer, E. S. Complex thermoelectric materials. *Nat. Mater.* **2008**, *7*, 105−114.

(2) Su, X.; Wei, P.; Li, H.; Liu, W.; Yan, Y.; Li, P.; Su, C.; Xie, C.; Zhao, W.; Zhai, P.; Zhang, Q.; Tang, X.; Uher, C. Multi-scale microstructural thermoelectric materials: transport behavior, non-equilibrium preparation, and applications. *Adv. Mater.* **2017**, *29*, 1602013.

(3) Zhang, Q. H.; Huang, X. Y.; Bai, S. Q.; Shi, X.; Uher, C.; Chen, L. D. Thermoelectric devices for power generation: recent progress and future challenges. *Adv. Eng. Mater.* **2016**, *18*, 194−213.

(4) Hsu, K. F.; Chung, D. Y.; Lal, S.; Mrotzek, A.; Kyratsi, T.; Hogan, T.; Kanatzidis, M. G. $CsMBi_3Te_6$ and $CsM_2Bi_3Te_7$ (M = Pb, Sn): New thermoelectric compounds with low-dimensional structures. *J. Am. Chem. Soc.* **2002**, *124*, 2410−2411.

(5) (a) Zhao, L. D.; He, J. Q.; Hao, S. Q.; Wu, C. I.; Hogan, T. P.; Wolverton, C.; Dravid, V. P.; Kanatzidis, M. G. Raising the Thermoelectric Performance of p-Type PbS with Endotaxial Nanostructuring and Valence-Band Offset Engineering Using CdS and ZnS. *J. Am. Chem. Soc.* **2012**, *134* (39), 16327−16336. (b) Ahn, K.; Han, M. K.; He, J. Q.; Androulakis, J.; Ballikaya, S.; Uher, C.; Dravid, V. P.; Kanatzidis, M. G. Exploring Resonance Levels and Nanostructuring in the PbTe-CdTe System and Enhancement of the Thermoelectric Figure of Merit. *J. Am. Chem. Soc.* **2010**, *132* (14), 5227−5235. (c) He, J. Q.; Sootsman, J. R.; Girard, S. N.; Zheng, J. C.; Wen, J. G.; Zhu, Y. M.; Kanatzidis, M. G.; Dravid, V. P. On the Origin of Increased Phonon Scattering in Nanostructured PbTe Based Thermoelectric Materials. *J. Am. Chem. Soc.* **2010**, *132* (25), 8669−8675.

(6) Biswas, K.; He, J.; Zhang, Q.; Wang, G.; Uher, C.; Dravid, V. P.; Kanatzidis, M. G. Strained endotaxial nanostructures with high thermoelectric figure of merit. *Nat. Chem.* **2011**, *3*, 160−166.

(7) Biswas, K.; He, J.; Blum, I. D.; Wu, C.-I.; Hogan, T. P.; Seidman, D. N.; Dravid, V. P.; Kanatzidis, M. G. High-performance bulk thermoelectrics with all-scale hierarchical architectures. *Nature* **2012**, *489*, 414−418.

(8) Wu, H. J.; Zhao, L. D.; Zheng, F. S.; Wu, D.; Pei, Y. L.; Tong, X.; Kanatzidis, M. G.; He, J. Q. Broad temperature plateau for thermoelectric figure of merit ZT > 2 in phase-separated $PbTe_{0.7}S_{0.3}$. *Nat. Commun.* **2014**, *5*, 4515.

(9) Wei, T. R.; Tan, G. J.; Zhang, X. M.; Wu, C. F.; Li, J. F.; Dravid, V. P.; Snyder, G. J.; Kanatzidis, M. G. Distinct impact of alkali-ion doping on electrical transport properties of thermoelectric p-type polycrystalline SnSe. *J. Am. Chem. Soc.* **2016**, *138*, 8875−8882.

(10) Mrotzek, A.; Chung, D. Y.; Ghelani, N.; Hogan, T.; Kanatzidis, M. G. Structure and thermoelectric properties of the new quaternary bismuth selenides $A_{1\text{-}x}M_{4\text{-}x}Bi_{11+x}Se_{21}$ (A = K and Rb and Cs; M = Sn and Pb) - Members of the grand homologous series $K_m(M_6Se_8)_m(M_{5+n}Se_{9+n})$. *Chem. - Eur. J.* **2001**, *7*, 1915−1926.

(11) Mrotzek, A.; Iordanidis, L.; Kanatzidis, M. G. $Cs_{1-x}Sn_{1-\underline{x}}Bi_{9+x}Se_{15}$ and $Cs_{1.5-3x}Bi_{9.5+x}Se_{15}$: members of the homologous superseries $A_m[M_{1+l}Se_{2+l}]_{2m}[M_{1+2l+n}Se_{3+3l+n}]$(A = alkali metal, M= Sn and Bi) allowing structural evolution in three different dimensions. *Chem. Commun.* **2001**, *17*, 1648−1649.

(12) Hoang, K.; Tomic, A.; Mahanti, S. D.; Kyratsi, T.; Chung, D. Y.; Tessmer, S. H.; Kanatzidis, M. G. Role of K/Bi disorder in the electronic structure of beta-$K_2Bi_8Se_{13}$. *Phys. Rev. B: Condens. Matter Mater. Phys.* **2009**, *80*, 125112.

(13) Chung, D. Y.; Uher, C.; Kanatzidis, M. G. Sb and Se substitution in $CsBi_4Te_6$: The semiconductors CsM_4Q_6 (M = Bi, Sb; Q = Te, Se), $Cs_2Bi_{10}Q_{15}$, and $CsBi_5Q_8$. *Chem. Mater.* **2012**, *24*, 1854−1863.

(14) Ohta, M.; Chung, D. Y.; Kunii, M.; Kanatzidis, M. G. Low lattice thermal conductivity in $Pb_5Bi_6Se_{14}$, $Pb_3Bi_2S_6$, and $PbBi_2S_4$: promising thermoelectric materials in the cannizzarite, lillianite, and galenobismuthite homologous series. *J. Mater. Chem. A* **2014**, *2*, 20048−20058.

(15) James, D. J.; Lu, X.; Morelli, D. T.; Brock, S. L. Solvothermal synthesis of tetrahedrite: Speeding up the process of thermoelectric material generation. *ACS Appl. Mater. Interfaces* **2015**, *7*, 23623−23632.

(16) Lu, X.; Morelli, D.; Xia, Y.; Zhou, F.; Ozolins, V.; Chi, H.; Zhou, X.; Uher, C. High Performance Thermoelectricity in Earth-Abundant Compounds Based on Natural Mineral Tetrahedrites. *Adv. Energy Mater.* **2013**, *3*, 342−348.

(17) Perez-Mato, J.; Elcoro, L.; Makovicky, E.; Topa, D.; Petříček, V.; Madariaga, G. Conspicuous variation of the lattice unit cell in the pavonite homologous series and its relation with cation/anion occupational modulations. *Mater. Res. Bull.* **2013**, *48*, 2166−2174.

(18) Xia, Z.; Poeppelmeier, K. R. Chemistry-inspired adaptable framework structures. *Acc. Chem. Res.* **2017**, *50*, 1222−1230.

(19) Anglin, C.; Takas, N.; Callejas, J.; Poudeu, P. F. Crystal structure and physical properties of the quaternary manganese-bearing pavonite homologue $Mn_{1.34}Sn_{6.66}Bi_8Se_{20}$. *J. Solid State Chem.* **2010**, *183*, 1529−1535.

(20) Wang, M.-F.; Jang, S.-M.; Huang, J.-C.; Lee, C.-S. Synthesis and characterization of quaternary chalcogenides InSn2Bi3Se8 and In0.2Sn6Bi1.8Se9. *J. Solid State Chem.* **2009**, *182*, 1450−1456.

(21) Tan, G.; Hao, S.; Zhao, J.; Wolverton, C.; Kanatzidis, M. G. High thermoelectric performance in electron-doped $AgBi_3S_5$ with ultralow thermal conductivity. *J. Am. Chem. Soc.* **2017**, *139*, 6467−6473.

(22) *X-AREA, X-RED, and X-SHAPE*; Cie & Stoe: Darmstadt, Germany, 1998.

(23) Sheldrick, G. A short history of SHELX. *Acta Crystallogr., Sect. A: Found. Crystallogr.* **2008**, *64*, 112−122.

(24) de Boor, J.; Gupta, S.; Kolb, H.; Dasgupta, T.; Muller, E. Thermoelectric transport and microstructure of optimized $Mg_2Si_{0.8}Sn_{0.2}$. *J. Mater. Chem. C* **2015**, *3*, 10467−10475.

(25) Kim, H. S.; Gibbs, Z. M.; Tang, Y.; Wang, H.; Snyder, G. J. Characterization of Lorenz number with Seebeck coefficient measurement. *APL Mater.* **2015**, *3*, 041506.

(26) Perdew, J. P.; Burke, K.; Ernzerhof, M. Generalized gradient approximation made simple. *Phys. Rev. Lett.* **1996**, *77*, 3865−3868.

(27) Kresse, G.; Furthmüller, J. Efficient iterative schemes for ab initio total-energy calculations using a plane-wave basis set. *Phys. Rev. B: Condens. Matter Mater. Phys.* **1996**, *54*, 11169−11186.

(28) Zhao, L. D.; Lo, S. H.; Zhang, Y.; Sun, H.; Tan, G.; Uher, C.; Wolverton, C.; Dravid, V. P.; Kanatzidis, M. G. Ultralow thermal conductivity and high thermoelectric figure of merit in SnSe crystals. *Nature* **2014**, *508*, 373−377.

(29) Morelli, D. T.; Heremans, J. P.; Slack, G. A. Estimation of the isotope effect on the lattice thermal conductivity of group IV and

group III-V semiconductors. *Phys. Rev. B: Condens. Matter Mater. Phys.* **2002**, *66*, 195304.

(30) Asen-Palmer, M.; Bartkowski, K.; Gmelin, E.; Cardona, M.; Zhernov, A.; Inyushkin, A.; Taldenkov, A.; Ozhogin, V.; Itoh, K. M.; Haller, E. Thermal conductivity of germanium crystals with different isotopic compositions. *Phys. Rev. B: Condens. Matter Mater. Phys.* **1997**, *56*, 9431.

(31) Morelli, D.; Heremans, J.; Slack, G. Estimation of the isotope effect on the lattice thermal conductivity of group IV and group III-V semiconductors. *Phys. Rev. B: Condens. Matter Mater. Phys.* **2002**, *66*, 195304.

(32) Hao, S.; Shi, F.; Dravid, V. P.; Kanatzidis, M. G.; Wolverton, C. Computational prediction of high thermoelectric performance in hole doped layered GeSe. *Chem. Mater.* **2016**, *28*, 3218−3226.

(33) Zhang, Y.; Skoug, E.; Cain, J.; Ozoliņš, V.; Morelli, D.; Wolverton, C. First-principles description of anomalously low lattice thermal conductivity in thermoelectric Cu-Sb-Se ternary semiconductors. *Phys. Rev. B: Condens. Matter Mater. Phys.* **2012**, *85*, 054306.

(34) Kim, J.-H.; Chung, D.-Y.; Kanatzidis, M. G. A new chalcogenide homologous series $A_2[M_{5+n}Se_{9+n}]$(A = Rb, Cs; M = Bi, Ag, Cd). *Chem. Commun.* **2006**, *15*, 1628−1630.

(35) Casamento, J.; Lopez, J. S.; Moroz, N. A.; Olvera, A.; Djieutedjeu, H.; Page, A.; Uher, C.; Poudeu, P. F. P. Crystal structure and thermoelectric properties of the 7,7L Lillianite homologue $Pb_6Bi_2Se_9$. *Inorg. Chem.* **2017**, *56*, 261−268.

(36) Zhao, J.; Islam, S. M.; Kontsevoi, O. Y.; Tan, G.; Stoumpos, C. C.; Chen, H.; Li, R. K.; Kanatzidis, M. G. The two-dimensional $A_xCd_xBi_{4-x}Q_6$ (A = K, Rb, Cs; Q = S, Se): direct bandgap semiconductors and ion-exchange materials. *J. Am. Chem. Soc.* **2017**, *139*, 6978−6987.

(37) Makovicky, E.; Mumme, W.; Watts, J. The crystal structure of synthetic pavonite, $AgBi_3S_5$, and the definition of the pavonite homologous series. *Can. Mineral.* **1977**, *15*, 339−348.

(38) Mrotzek, A.; Kanatzidis, M. G. Tropochemical cell-twinning in the new quaternary bismuth selenides $K_xSn_{6-2x}Bi_{2+x}Se_9$ and $KSn_5Bi_5Se_{13}$. *Inorg. Chem.* **2003**, *42*, 7200−7206.

(39) Zhao, L.-D.; Zhang, X.; Wu, H.; Tan, G.; Pei, Y.; Xiao, Y.; Chang, C.; Wu, D.; Chi, H.; Zheng, L.; et al. Enhanced thermoelectric properties in the counter-doped SnTe system with strained endotaxial SrTe. *J. Am. Chem. Soc.* **2016**, *138*, 2366−2373.

(40) Tan, G.; Shi, F.; Hao, S.; Chi, H.; Bailey, T. P.; Zhao, L.-D.; Uher, C.; Wolverton, C.; Dravid, V. P.; Kanatzidis, M. G. Valence band modification and high thermoelectric performance in snte heavily alloyed with MnTe. *J. Am. Chem. Soc.* **2015**, *137*, 11507−11516.

(41) Pei, Y.; Tan, G.; Feng, D.; Zheng, L.; Tan, Q.; Xie, X.; Gong, S.; Chen, Y.; Li, J. F.; He, J. Integrating band structure engineering with all-scale hierarchical structuring for high thermoelectric performance in PbTe system. *Adv. Energy Mater.* **2017**, *7*, 1601450.

(42) Tan, G.; Shi, F.; Hao, S.; Zhao, L.-D.; Chi, H.; Zhang, X.; Uher, C.; Wolverton, C.; Dravid, V. P.; Kanatzidis, M. G. Non-equilibrium processing leads to record high thermoelectric figure of merit in PbTe-SrTe. *Nat. Commun.* **2016**, *7*, 12167.

(43) Fabini, D. H.; Laurita, G.; Bechtel, J. S.; Stoumpos, C. C.; Evans, H. A.; Kontos, A. G.; Raptis, Y. S.; Falaras, P.; Van der Ven, A.; Kanatzidis, M. G.; Seshadri, R. Dynamic stereochemical activity of the Sn^{2+} lone pair in perovskite $CsSnBr_3$. *J. Am. Chem. Soc.* **2016**, *138*, 11820−11832.

(44) Stoumpos, C. C.; Malliakas, C. D.; Peters, J. A.; Liu, Z.; Sebastian, M.; Im, J.; Chasapis, T. C.; Wibowo, A. C.; Chung, D. Y.; Freeman, A. J.; et al. Crystal growth of the perovskite semiconductor $CsPbBr_3$: a new material for high-energy radiation detection. *Cryst. Growth Des.* **2013**, *13*, 2722−2727.

(45) Lin, H.; Tan, G.; Shen, J. N.; Hao, S.; Wu, L. M.; Calta, N.; Malliakas, C.; Wang, S.; Uher, C.; Wolverton, C.; Kanatzidis, M. G. Concerted rattling in $CsAg_5Te_3$ leading to ultralow thermal conductivity and high thermoelectric performance. *Angew. Chem., Int. Ed.* **2016**, *55*, 11431−11436.

(46) Androulakis, J.; Todorov, I.; Chung, D. Y.; Ballikaya, S.; Wang, G. Y.; Uher, C.; Kanatzidis, M. Thermoelectric enhancement in PbTe with K or Na codoping from tuning the interaction of the light- and heavy-hole valence bands. *Phys. Rev. B: Condens. Matter Mater. Phys.* **2010**, *82*. DOI: 10.1103/PhysRevB.82.115209.

(47) Dughaish, Z. H. Lead telluride as a thermoelectric material for thermoelectric power generation. *Phys. B (Amsterdam, Neth.)* **2002**, *322*, 205−223.

(48) Sootsman, J. R.; Chung, D. Y.; Kanatzidis, M. G. New and old concepts in thermoelectric materials. *Angew. Chem., Int. Ed.* **2009**, *48*, 8616−8639.

(49) Li, C. W.; Hong, J.; May, A. F.; Bansal, D.; Chi, S.; Hong, T.; Ehlers, G.; Delaire, O. Orbitally driven giant phonon anharmonicity in SnSe. *Nat. Phys.* **2015**, *11*, 1063−1069.